Electromagnetic analysis, efficiency map and thermal analysis of an 80-kW IPM motor with distributed and concentrated winding for electric vehicle applications

ADRIAN MŁOT[1] ✉, MARIUSZ KORKOSZ[2], ANDRZEJ LECHOWICZ[1],
JERZY PODHAJECKI[3], STANISŁAW RAWICKI[3]

[1]Opole University of Technology
Poland
[2]Rzeszow University of Technology
Poland
[3]The Jacob of Paradies University
Poland
e-mail: a.mlot@po.edu.pl

Abstract: This paper presents a comparison of an AC radial flux interior permanent magnet (IPM) motor with the distributed winding (DW) and concentrated winding (CW). From time to time, manufacturers of electric vehicles change the design of electric motors, such changes may include changing the DW into CW and vice versa. A change to the winding in a radial permanent magnet synchronous motor may lead to a change in motor parameters during motor operation and /or change in the distribution of the magnetic field and thermal circuit of the electrical machine. The electromagnetic analysis, efficiency map, mechanical stress, and thermal analysis of the machine with the DW and CW are presented in this paper. This article describes the advantages and disadvantages of selected stator winding designs and helps understand manufacturers' designers how the DW and CW play a key role in achieving the designed motor's operational parameters such as continuous performance. Analyzing the performance of both machines will help identify their advantages and disadvantages with regard to thermal phenomena, magnetic field and operational parameters of the presented IPM prototypes. Both prototypes are based on commonly used topologies such as 12/8 (slot/pole) and 30/8 (slot/pole) IPM motors consisting of magnets arranged in a V-shape. The AC IPM motor was designed for an 80 kW propulsion system to achieve 170 N·m at a base speed of 4 500 rpm. Modern CAD tools are utilized throughout the numerical computations based on 2-D finite element methods. Selected test data are used to verify and validate the accuracy of finite element models.

Key words: AC losses, distributed and concentrated winding, motor performance, radial flux permanent magnet motor, slot fill factor, thermal analysis

1. Introduction

Despite the extensive evidence in the literature on the electromagnetic, thermal, mechanical stress and efficiency analysis of electric motors, research in this respect is repeated in detail when new prototypes of electrical machines are designed. Many academic publications discuss the electromagnetic analysis, thermal analysis and efficiency map separately [1–6] for AC permanent magnet propulsion motors. Also, many investigations were focused on the influence of winding design on iron/copper/PM losses in brushless PM motors using the DW or CW [7–10]. For the comparison of electric motors with the DW and CW, there is little guidance available [11–14]. Nevertheless, each new electric motor design requires comprehensive analysis, and the reason for that is that different operational parameters and construction dimensions are required for electric motors [15–20]. When developing a new electrical machine, it is important to perform a comprehensive analysis such as voltage waveforms induced in the armature winding and its total harmonic distortion (THD), power losses, electromagnetic torque and its pulsations, thermal analysis, efficiency map etc. [21–23].

In this paper, the authors present two prototypes with a topology based on an IPM radial flux motor with Nd-Fe-B magnets inserted in the rotor core. One prototype consists of a 12-slot 8-pole motor with the CW, and the second one consists of a 30-slot 8-pole motor with the DW. Based on the authors' knowledge and experience, a number of technical and economic requirements were taken into account, such as low noise level, high efficiency, material cost, and manufacturing constraints. These issues were described by the authors in [24]. In electric motors with a power of several dozen kilowatts and a relatively low supply voltage (several hundred volts) intended to drive electric vehicles, it is usually required to use a multi-wire winding. A multi-wire winding was also used in both analysed prototypes. According to the authors, the use of a multi-wire winding reduces the slot fill factor. It results in the deterioration of the electric motor parameters, regardless of the type of winding (e.g. increase in copper losses). The proposed 80 kW prototypes are based on designed and optimized motors similar to those described in [25–27]. It is commonly known that the stator winding distribution can have a profound influence on stator and rotor iron losses. In terms of these losses, the most common winding configurations are used in the presented prototypes. Of the many possible configurations for placing the magnets inside the core, the V-shape configuration was chosen. In addition, from an economic point of view, this configuration is most desirable and also a V-shape IPM motor has good performance in both torque and extended speed [27,28]. Presented IPM prototypes were widely investigated in relation to a winding short-circuit fault on demagnetization risk and local magnetic forces [29]. In this paper, the authors have decided to extend the study of the performance and thermal investigations in the proposed prototypes. Eighty kW prototypes are designed for a propulsion system achieving an electromagnetic torque of 170 N·m at base speed. These machines are widely used for electric and hybrid traction applications (in this particular project, IPM prototypes were designed for electric SUVs). Two electric motors of the same type installed in the car drive will propel the front and rear wheels. In electric vehicle propulsion, mechanical transmission occurs between plugs, the battery, charges and power converter, and electrical transmission occurs between the IPM AC motor and power converter. The motors are directly connected to the clutch, then to the transmission and gearbox, and then to the front differential.

The analysis performed should demonstrate the differences, advantages and disadvantages of the motor's operational parameters and point out the weakest areas of the constructed IPM

prototypes. The conclusions can be very useful to specify further modifications or optimization processes to develop a new motor prototype with improved parameters such as torque constant, voltage constant, cogging torque, torque ripple or efficiency and output power characteristics. In many automotive industry research units, engineers for different reasons change, from time to time, the topology of the electric motor and usually face several serious issues that must be sorted out. This paper demonstrates two different winding structures of the IPM motor to make it easier for engineers to choose a machine for specific applications and requirements.

The CW design (with the same size, and stator/rotor radius as in an IPM using the DW design) enables easy winding automation and has short end-windings, lower copper loss, and requires less space than the DW [30]. On the other hand, the use of the CW leads to a higher winding factor. One of the methods to improve the output torque of an IPM with the CW can be using unequal tooth width of the stator and an appropriate choice of slot and pole numbers. It has been proven in many studies that the DW with a high number of slots has a lower cogging torque, and also higher resistance to mechanical deformation than an IPM motor with the CW [30]. Also, an electric motor with a CW motor can generate less copper and iron losses than a machine with the DW operating in the constant power region [30], while in the constant torque region, the losses in both machines can be similar. However, the researchers are concerned only with specific problems such as electromagnetic analysis, improvement of output power, achieving high efficiency etc. Only a small amount of academic literature discusses widely the advantages and disadvantages of using distributed and concentrated windings based on monitoring its performance and thermal and mechanical analysis or at least demonstrates the necessity to perform thermal analysis and address the related design problems. To bridge this gap, the authors conducted the necessary research to present a comprehensive view of the comparison of an IPM motor with the DW and CW used for automotive applications, and the conclusions should help engineers select the right motor topology depending on their requirements. In the analysis performed, the influence of additional AC losses in the motor windings was taken into account. The authors argue that additional AC losses significantly affect the temperature distribution in the electric motor. Failure to take into account AC losses significantly limits the maximum performance of the designed machines operating in the range of constant power. According to the authors, the method/technology used for making the winding plays an important role, which will be shown in the paper.

2. Experimental validation of finite element analysis and electromagnetic analysis

Designed IPM prototypes combine high performance with low-cost production, but without the light weight or small size that are ideal for electric or hybrid SUVs. Reducing production costs with the simultaneous use of a multi-wire winding requires reducing the slot filling factor by several percent. It is not possible to obtain a slot filling factor of 70–75% with the use of a multi-wire winding without incurring additional costs at the stage of the winding of the stator. Relatively low supply voltage (400 VDC) and high power (80 kW) require the use of a multi-wire winding (for skin effect elimination). Additionally, the cross-section of the winding wire limits the opening of the slot space. Typically, the winding wire cross-section should be less than about 3 times the width of the slot opening.

A cross-sectional view of the prototypes is shown in Fig. 1(a). The main dimensions and the layout of the winding arrangements with the laminated core sheets are presented in Figs. 1(b)–1(c). Due to the difference in the number of poles and slots for both IPM motors, it was necessary to change the inside diameter of the stator and thus change the outside diameter of the rotor. Moreover, minimizing the cogging torque to an acceptable level required changing the arrangement of the permanent magnets. Additionally, both motor designs had to have comparable voltage constants. Consequently, despite the use of a V-shape magnet system, this system is slightly different in both solutions. These prototypes included V-shaped interior PMs arranged in simple rectangular magnet blocks that allow to reduce machining costs (there were six magnet segments in the axial direction). Furthermore, the shape of the magnetic flux barrier designed in the rotor core is simple and ensures an acceptable flux density distribution around this barrier. Also, the flux passing through the air gap assures a low total harmonic distortion of the back electromotive force.
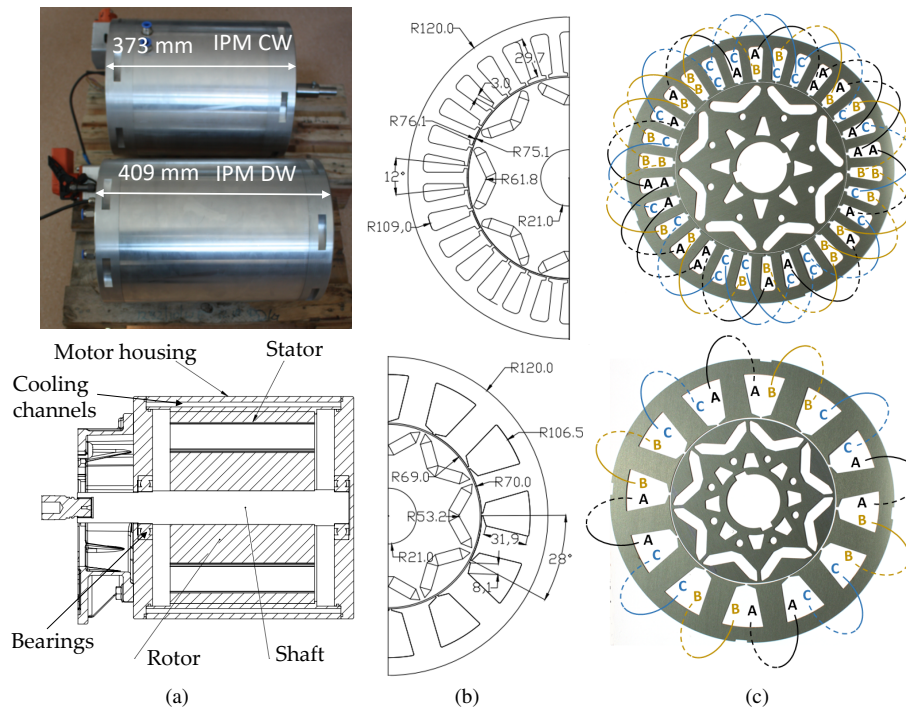

Fig. 1. 30/8 and 12/8 IPM motors: 80 kW IPM AC motor prototypes used in the electric vehicle drive with a 3D view and a cross-sectional view (a); dimensions (b); radial view of the DW and CW layout and the coil mounted in a 3-phase stator (c)

The tested machines should be capable of delivering a nominal power of 80 kW when driven by an inverter with sinusoidal voltage with controllable frequency and amplitude (load operation be tested in the near future). The tested three-phase IPM prototypes based on radial flux technology that were set in the test rig are shown in Fig. 2. A comparison between the data from the numerical calculations based on the finite element method/analysis (FEM/FEA) and the experiment involving

the cogging torque, Back-EMF, and the electro-magnetic static torque show a good agreement. The commercially available software based on the FEM was used to design and investigate the geometry of the IPM motors. The shaft of the prototype was directly coupled with a flexible coupling, and then to the driving machine. A test-stand application with a multichannel data acquisition system programmed in LabView was used for electric machine operational parameter measurements. For the static characteristics of electromagnetic torque measurements, the AC drive motor was used and directly coupled with flexible couplings, torque transducer, and IPM motor. For precise measurements of the cogging torque, a stepper motor with a planetary gear was used instead of an AC drive motor. When the Back-EMF was measured, the stepper motor was replaced with a load machine to spin the IPM motor with the required speed.
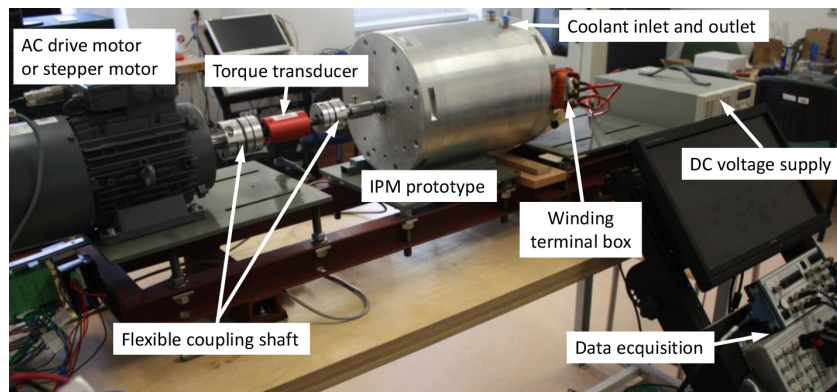

Fig. 2. The test rig with an IPM motor prototype used for torque and Back-EMF measurements

Several parameters representing general specifications for the test motors were set, as is typical for most design projects, see Table 1. Table 1 also includes information on the windings used. The outer diameter of the stator in both machines is 240 mm.

Measurement of the waveform of BEMF generated by the electric motor is one of the most important parameters that must be compared with the one simulated using the FEA. The convergence of the results should be as high as possible in order to confirm the correctness of the numerical model for the analysis of the magnetic field and integral parameters of electric motors. The test of no-load BEMF (phase-to-neutral voltage) was performed at 4 500 rpm and it is presented in Fig 3. The phase BEMF conveys the most important information as its distortion directly causes torque ripple. Also, it can be observed that with the decreasing number of slots per pole and changing the winding type from the DW to CW, the waveform is more trapezoidal and consists of more little ripples.

Observation of the line-to-line BEMF (between two phases) is important in most cases as the star connection of electric machines. Those line-to-line voltage waveforms are important to estimate voltage distortion in star connection, see Fig. 4. The line-to-line voltage waveforms of the DW electric machine are smoother than those of phase BEMF. In the case of the CW electric machine, the line-to-line BEMF waveforms are slightly flattened at the top of the sine waves and have almost the same shape. In the case of an IPM motor with the DW, it can be concluded that the 30-pole configuration may be useful for the BLDC machine also in the star connection.

Table 1. Details of a prototype three-phase IPM with DW and CW

Parameter	IPM with DW	IPM with CW	Unit
Rated speed	4 500	4 500	rpm
Nominal torque	170	170	N·m
Rated power	80	80	kW
DC voltage	400	400	V
Number of stator slots/rotor poles	30/8	12/8	–
Iron core material	M270-35A	M270-35A	–
Iron core electrical resistivity	52	52	$\mu\Omega$·cm
Magnet width	17.6	18.9	elec.deg.
Magnet thickness	7.8	8.6	mm
Magnet grade	N38UH	N38UH	–
Magnet electrical resistivity	180	180	$\mu\Omega$·cm
Air gap length	1	1	mm
Stator/rotor outer diameter	240/150.2	240/138	mm
Stator/rotor inner diameter	152.2/42	140/42	mm
Slot height/pitch	29.7/12	31.9/28	mm/meh.deg.
Slot opening	2	2	mm
Yoke height	11	13.5	mm
Winding layers	Double-layer	Single-layer	–
Overlapping	Yes	No	–
Parallel paths	1	4	–
Winding throw	4	1	–
Winding factors	0.902	0.866	–
Wire slot fill	0.5	0.52	–
Copper slot fill	0.4	0.4	–
Strands in hand	Yes	Yes	–
Phase resistance	0.006835	0.00512	Ω
Armature turns per phase/coil	20/2	76 /19	–

Total harmonic distortion (THD) is a measure of how many of all the harmonics, except the fundamental ones, there are. THD can be expressed by the formula described below.

$$\text{THD} = \frac{\sqrt{\sum_{n=2}^{\infty} \text{BEMF}_n^2}}{\text{BEMF}_{n=1}} \cdot 100\%, \tag{1}$$
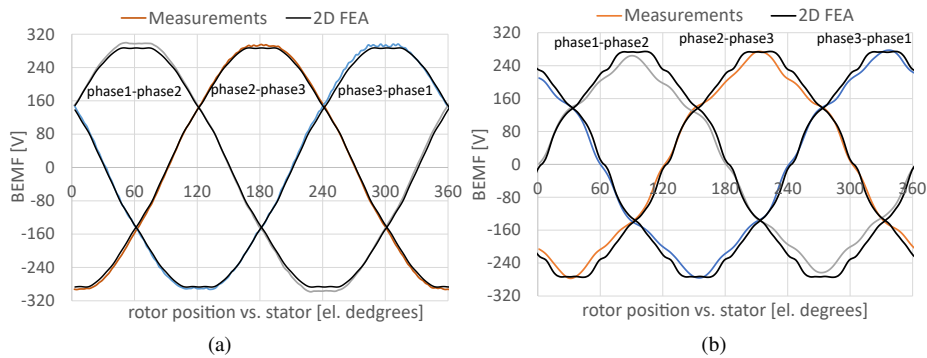
Fig. 3. No-load line-to-neutral BEMF waveforms at 4 500 rpm comparison between measurements and 2d FEA for prototypes with DW (a) and with CW (b)
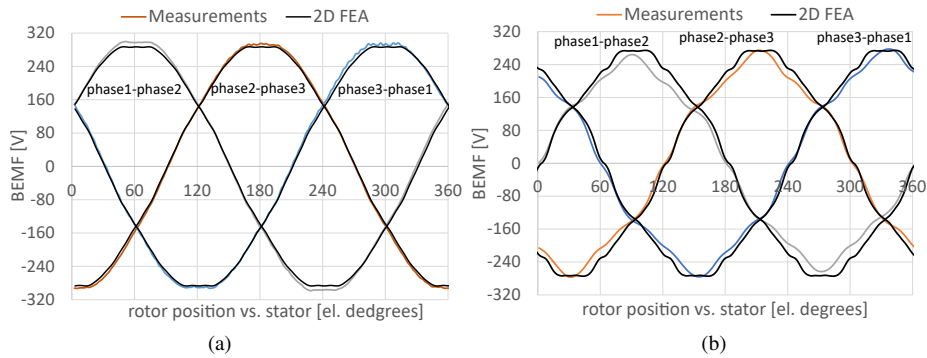

Fig. 4. Line-to-line BEMF voltage of DW (a), and CW (b) electric machine at 4 500 rpm

where $BEMF_n$ is the rms value of the n-th harmonic voltage representing amplitudes of all harmonics except the signal harmonics and $|BEMF_{n=1}|$ is the amplitude of the signal in this case, the signal is the fundamental frequency. By analyzing the THD of the phase-to-neutral BEMF waveform, it can be confirmed that the DW has less harmonic distortion (THD = 3.42%) and is most suitable for synchronous drives than the electric machine with the CW (THD = 5.65%). In line-to-line BEMF voltage, it can be observed that the 12-slot motor has far more distorted waveforms (THD = 4.9%) than the DW machine (THD 2.08%).

During the test, the coolant system was not used, and in the FEA, the temperature was assumed to be 25°C. To avoid a significant impact of the heat transfer on the torque production at varying loads and efficiencies of PM motors using NdFeB magnets, the measurements were performed quickly and at the same room temperature (25°C). As it was measured in detail in [29], the measured peak cogging torque was 0.87 N·m and 1.25 N·m (the higher value applies to the CW IPM motor). At the same time, the obtained measurements were sufficiently convergent compared to the calculated values of the cogging torque for the DW and CW, and the difference was not greater than 2% and 16%, respectively. Electromagnetic torque T_e static characteristics at load conditions were only partially verified (see Fig. 5). As it can be seen, more deformation of the

torque wave was observed for the IPM motor with the CW when compared to the one with the DW (see Fig. 5(b)). From the static characteristics of the torque, the DW motor generates a lower torque ripple than the machine with a lower number of slots. For both versions of IPM motors, the increase in current causes a decrease in the THD value of electromagnetic torque, as follows: for the DW – 9.32% (30 A), 10.11% (20 A), 15.28% (10 A), and for the CW – 9.32% (30 A), 10.10% (20 A), 15.26% (10 A). As can be seen, the THD factor of the torque does not differ significantly between both machines, nevertheless, the shape of the deformation characteristics between the two machines differs significantly. A detailed analysis of the electromagnetic torque at sinusoidal current load operation is also shown in [29], where it was observed that a DW IPM motor has a higher torque constant and a lower torque ripple.
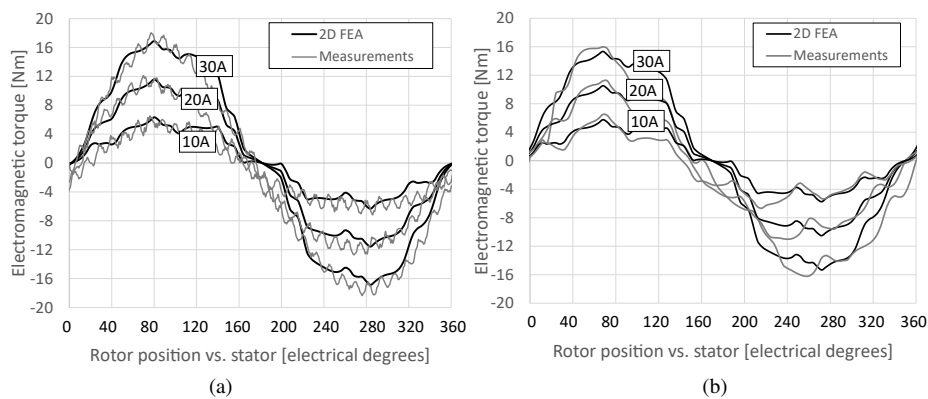

Fig. 5. Static characteristics of electromagnetic torque at load operation, IPM motor with:
DW (a) and CW (b)

Electromagnetic torque T_e is calculated using the virtual work method which is based on the stored magnetic co-energy change with a small displacement θ. T_e equals the derivative of the magnetic co-energy $W_{co\text{-}eng}$ with respect to the angular position at constant current, and is expressed as:

$$T_e = \left.\frac{\Delta W_{co\text{-}eng}}{\Delta \theta}\right|_{I=const}. \tag{2}$$

Figure 6(a) shows torque ripple factor ε expressed as a percentage, average value of the waveform of T_{av}, and torque constant k_T at the rms load current for each tested electric motor. Additionally, k_T is defined as [23]:

$$k_T = \frac{T_{av}}{I}, \tag{3}$$

where: k_T is the torque constant in N·m/A, I is the rms current in A and T_{av} is the electromagnetic average torque in N·m obtained for each AF PMSM. Torque ripple factor can be expressed as follows:

$$\varepsilon = \frac{T_{max} - T_{min}}{T_{av}} 100\%, \tag{4}$$

where T_{max}, T_{min}, represent the maximum and minimum value of the electromagnetic torque waveform as illustrated in Fig. 6(b).
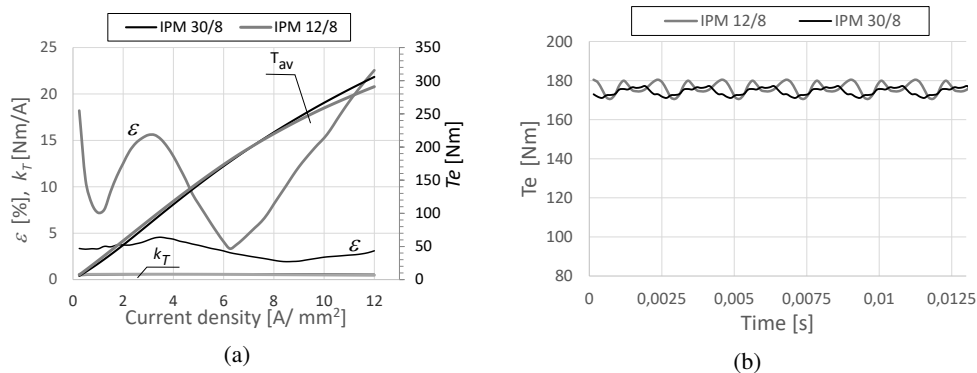
Fig. 6. Comparison of selected IPM motor parameters with DW and CW: torque ripple factor, torque constant, and average electromagnetic torque vs. rms load current (a); an example of the waveform of electromagnetic torque at 6.1 A/mm^2 (b)

In the range of normal IPM motor operation, no significant change in the torque constant was observed.

3. Efficiency maps

The expected operating range of the designed drive has been limited to 11 000 rpm. The presented IPM electric motor should operate in an overload condition for brief periods when it is required. The value of the permissible overload is determined by the value of the maximum current drawn from the battery bank. Assuming that the battery packs allow one to temporarily increase the value of the current (this occurs when the vehicle accelerates rapidly or the drive system is difficult to start), the characteristics of the maximum torque that can be obtained in the analyzed IPM prototypes can be determined. Thus, the relationship between the torque on the motor shaft, the output power and the efficiency of the motor as a function of rotational speed were determined for IPMs with the DW and those with the CW. It was assumed that in the analyzed drive system it is possible to temporarily double the maximum value of the motor current ($J = 12.2$ A/mm^2).

For a proper comparison of the characteristics of both prototypes, it is important to take into account AC losses in stator windings [31, 32]. The AC losses in the windings due to the proximity effect depend on [33]:

$$P_{\mathrm{AC}} = l_{\mathrm{Fe}} \frac{\pi d_c^2 \sigma (\omega B)^2}{124} \,, \tag{5}$$

where: l_{Fe} is the active length of the conductors, B is the flux density of the sinusoidal external field, ω is the angular frequency, σ is the electrical conductivity and d_c is the conductor diameter.

These losses are particularly important for machines operating in the range of constant power (the field weakening region). The authors attribute AC losses to the configuration of the winding, i.e. the position of individual turns in the slot or the number of wires in the bundle [34]. When eddy currents occur within the copper conductors, they become the source of the important phenomenon

of proximity effect. The proximity effect occurs because of increased frequency and/or load of the current. Therefore, it is very important to take into account the AC losses, especially in structures with windings with multi-wire coils (analyzed prototype structures presented in this article). And proximity losses can be predicted by using the real Joule effect formula considering the effective AC resistance R_{AC} and the real DC resistance R_{DC} [34, 35]. The bulk value of resistance as a function of power loss P_{cu} and the rms current determines the increase of resistance under AC excitation as compared to DC operations. If necessary, AC resistance can be calculated from the Joule loss of winding coils:

$$P_{cu} = \iint_V E \cdot J \, dV = \rho \iint_V J^2 \, dV = l_{Fe} \rho \iint_S J^2 \, dS, \tag{6}$$

where: E is the electric field strength, ρ is the resistivity of copper.

For comparison, the characteristics obtained for typical operating conditions ($J = 6.1$ A/mm^2) are computed. The relationship between the torque on the motor shaft, the output power and the efficiency of the motor is shown in Fig. 7. The characteristics were determined assuming a constant temperature of the stator winding (150°C) and permanent magnets (100°C).
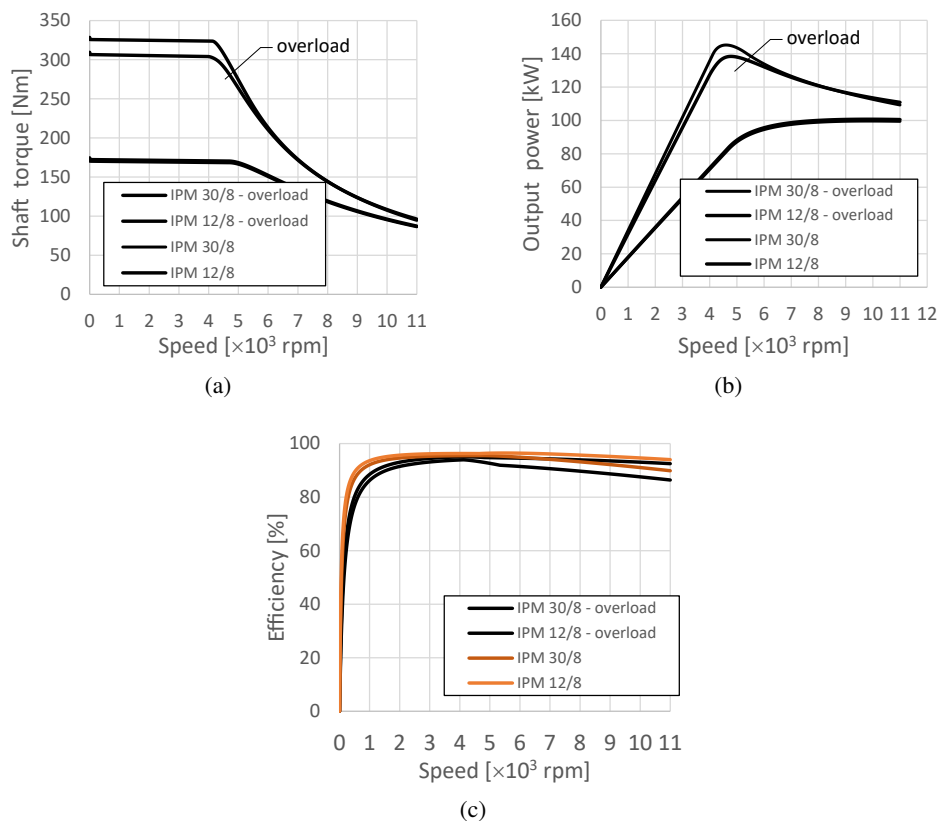

Fig. 7. FEA of selected parameters of IPM motor with DW and CW, operation at maximum current and overload: shaft torque vs. speed (a); output power vs. speed (b); efficiency vs. speed (c)

From Fig. 7, it can be concluded that the 12/8 structure has a lower overload capacity of 1.77 (1.93 for 30/8). The design 30/8 achieves greater maximum power. However, in terms of work with a constant power region (field weakening), the 12/8 design has much better parameters (taking into account thermal limitations), i.e. a wider speed range and higher efficiency. Additionally, it has a slightly higher efficiency in terms of constant torque operation. Also, the efficiency of the electric motor at constant power operation is significantly higher. This is important when the motor is operating in the field weakening zone.

Figures 8 and 9 show the efficiency maps computed using commercially available software [31–35] at the motor operation mode for a motor design with 12/8 and 30/8 poles, respectively. When determining the efficiency maps, it was assumed that a temporary twofold increase in motor current density is permissible. In the numerical calculations used, two control strategies are possible and were compared, i.e. a strategy aimed at maximizing the T/I_{rms} ratio or one
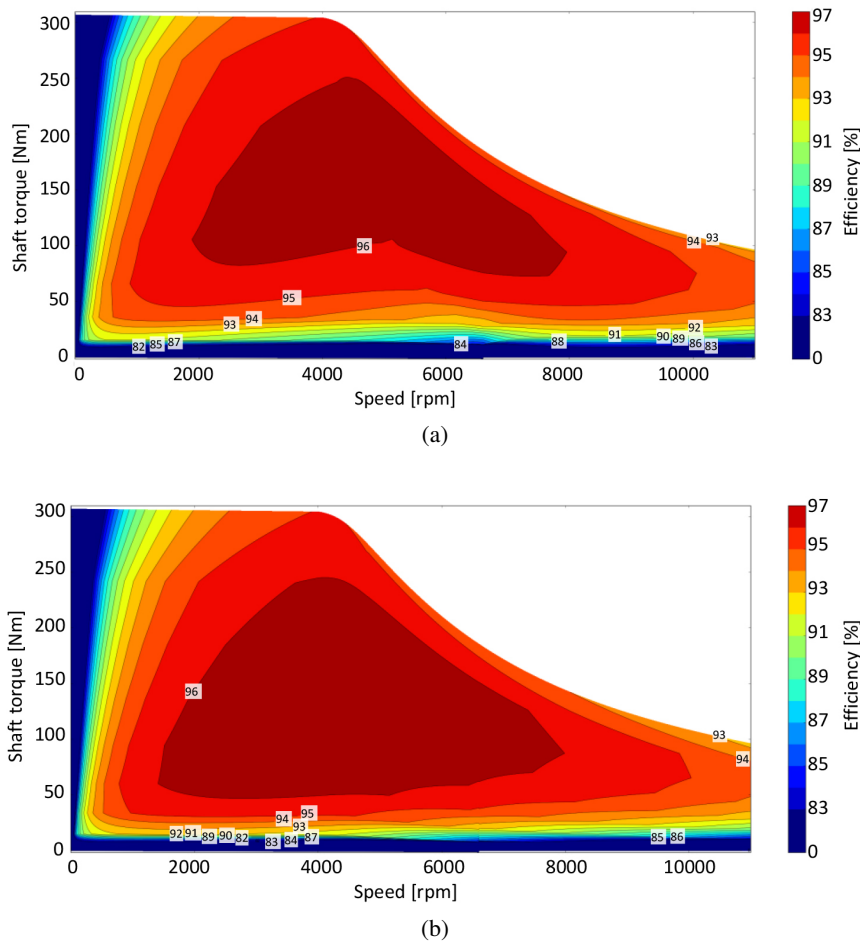

(a)

(b)

Fig. 8. Efficiency map of the 12/8 IPM motor: for the T/I_{rms} control strategy (a); for the control strategy based on maximum efficiency (b)

aimed at maximizing efficiency [35]. It is also possible to use the control strategy based only on maximizing the torque produced (not used in the calculations considered in this paper).

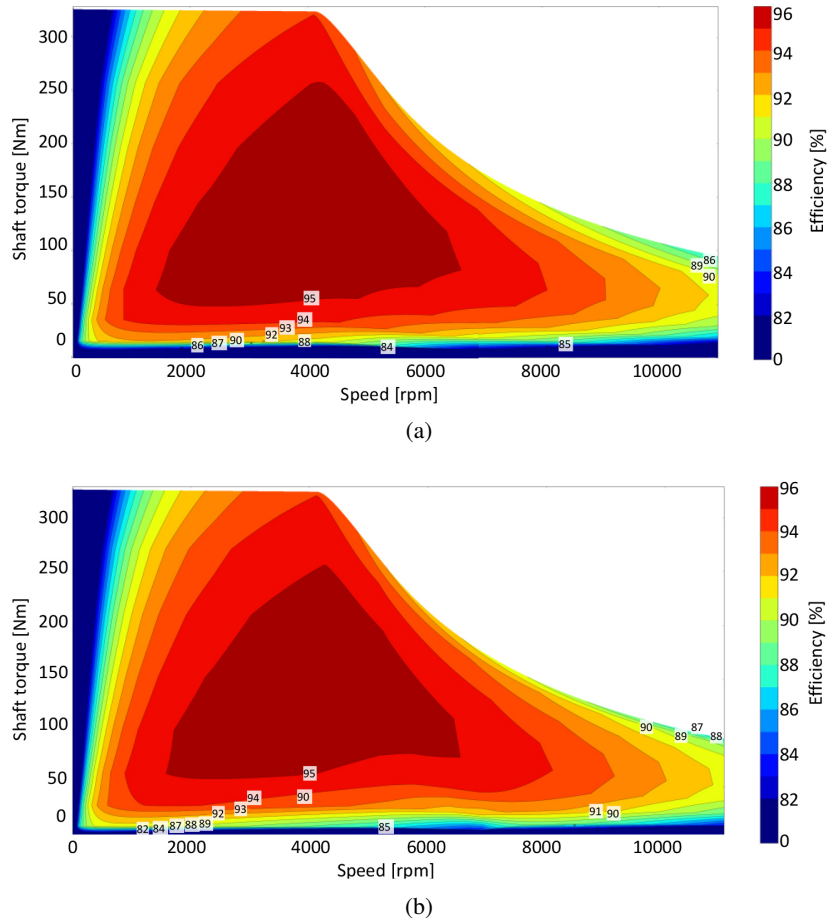The obtained maps of efficiency confirm the higher efficiency of the 12/8 construction.

(a)

(b)

Fig. 9. Efficiency map of the 30/8 IPM motor: for the T/I_{rms} control strategy (a); for the control strategy based on maximum efficiency (b)

4. Mechanical stress analysis

In terms of mechanical limitations, IPM-type motors are much less problematic than rotors with surface-mounted magnets [36]. However, due to the change in electric motor operation, e.g. from the constant torque zone to the constant power (field weakening) zone, it should be ensured that the maximum stresses in the rotor do not exceed the permissible values. In the case of rotors with internally mounted magnets, particular attention should be paid to the stresses in the magnetic

gap between rotor slots. From an electromagnetic point of view, the thickness of rotor magnetic flux barriers at the air gap must be suitably designed and not be too thick. However, when working in the field weakening range, the rotational speed of the rotor increases significantly, which causes an increase in stresses in the entire rotor. If magnetic bridges in the rotor (in magnetic flux barrier regions) are too thin, they become particularly susceptible to over-stresses. Figure 10 shows the stress distribution for the motors with the CW and DW at a maximum speed of 11 000 rpm.

(a)   (b)
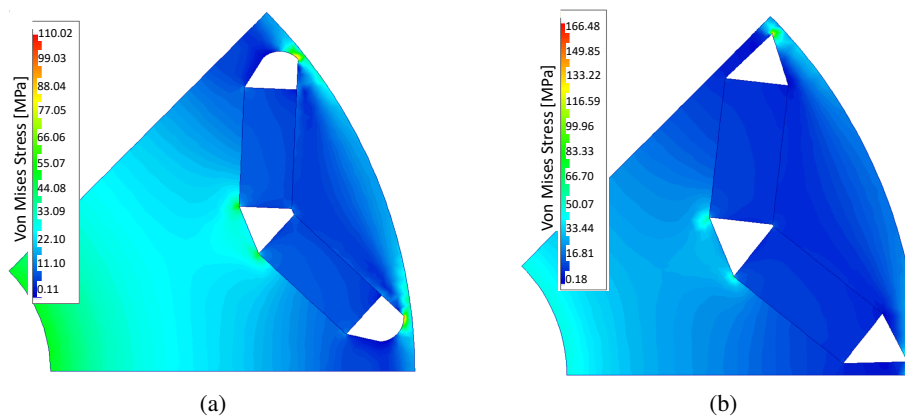
Fig. 10. Mechanical stress at the max. speed of 11 000 rpm: IPM with DW (a); IPM with CW (b)

From the analysis of stress distribution, it can be seen that both analyzed IPM structures allow the motors to operate in the required speed control range. The rotor's safety factor is high for both IPM motor designs. The rotor of the 30/8 design shows a higher safety factor (smaller volume of permanent magnets used) compared to the 12/8 motor design.

5. Thermal network and temperature distribution analysis

In the motors under consideration, as well as all-electric machines used in electric and hybrid vehicles, temperature has a key influence on stator windings and permanent magnets. In both cases, exceeding the permissible temperature for these elements has catastrophic consequences. Due to the high power density per unit volume, the machines are provided with forced cooling. In the thermal model, the stator housing with channels through which the coolant flows is designed and taken into account (the cooling channels can be seen in Fig 1(a)). The calculations analysed below were made using commercially available software [35–37] and were carried out for the thermally steady state and for motor operation at rated parameters (4 500 rpm, 170 N·m). The ambient temperature was set to 40°C, and the inlet temperature of the coolant system was set to 50°C. For the rated operating point of the motor, it is more important to control and analyse the temperature of stator windings. Moreover, a problem with the temperature of permanent magnets may appear in the working zone at the flux weakening field (above the rated speed). The calculations were performed as co-simulation between the electromagnetic and thermal modules. The results of the thermal analysis for the required operating point are shown in Figs. 11–13.
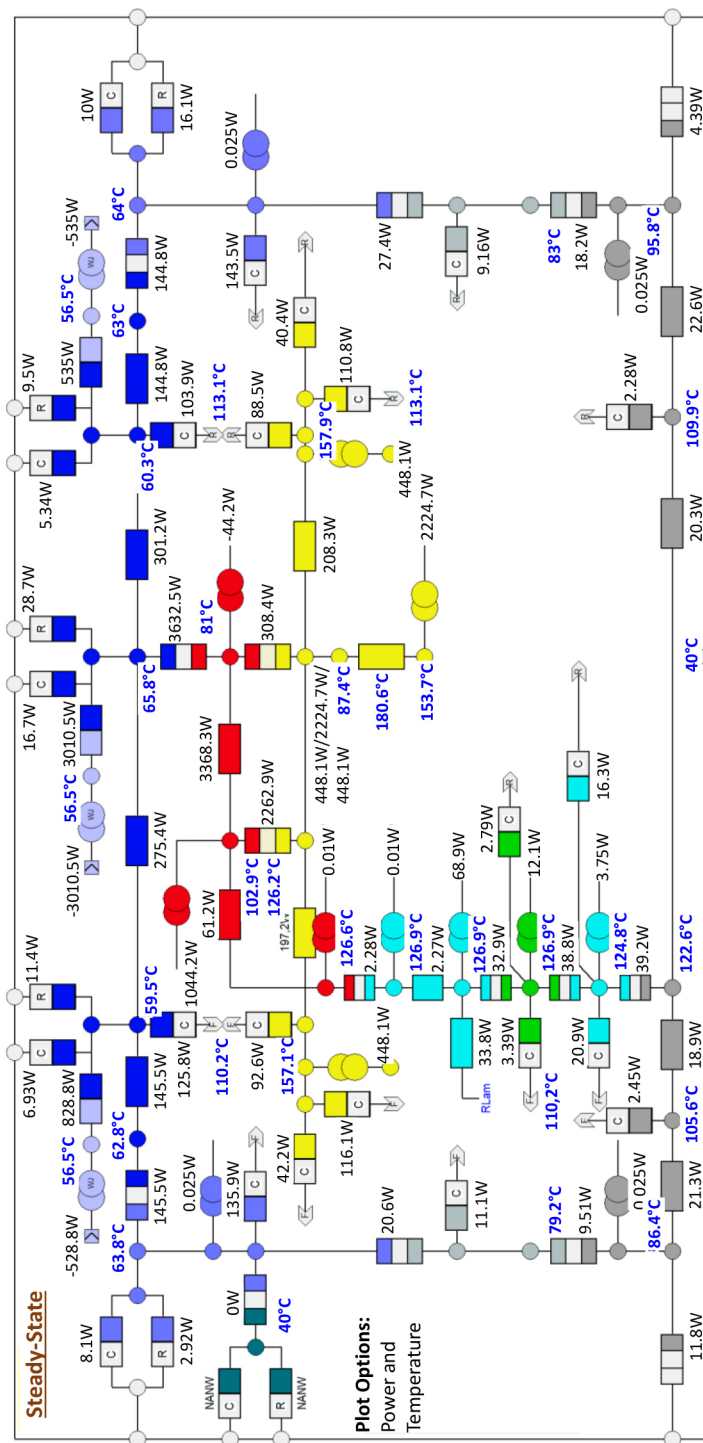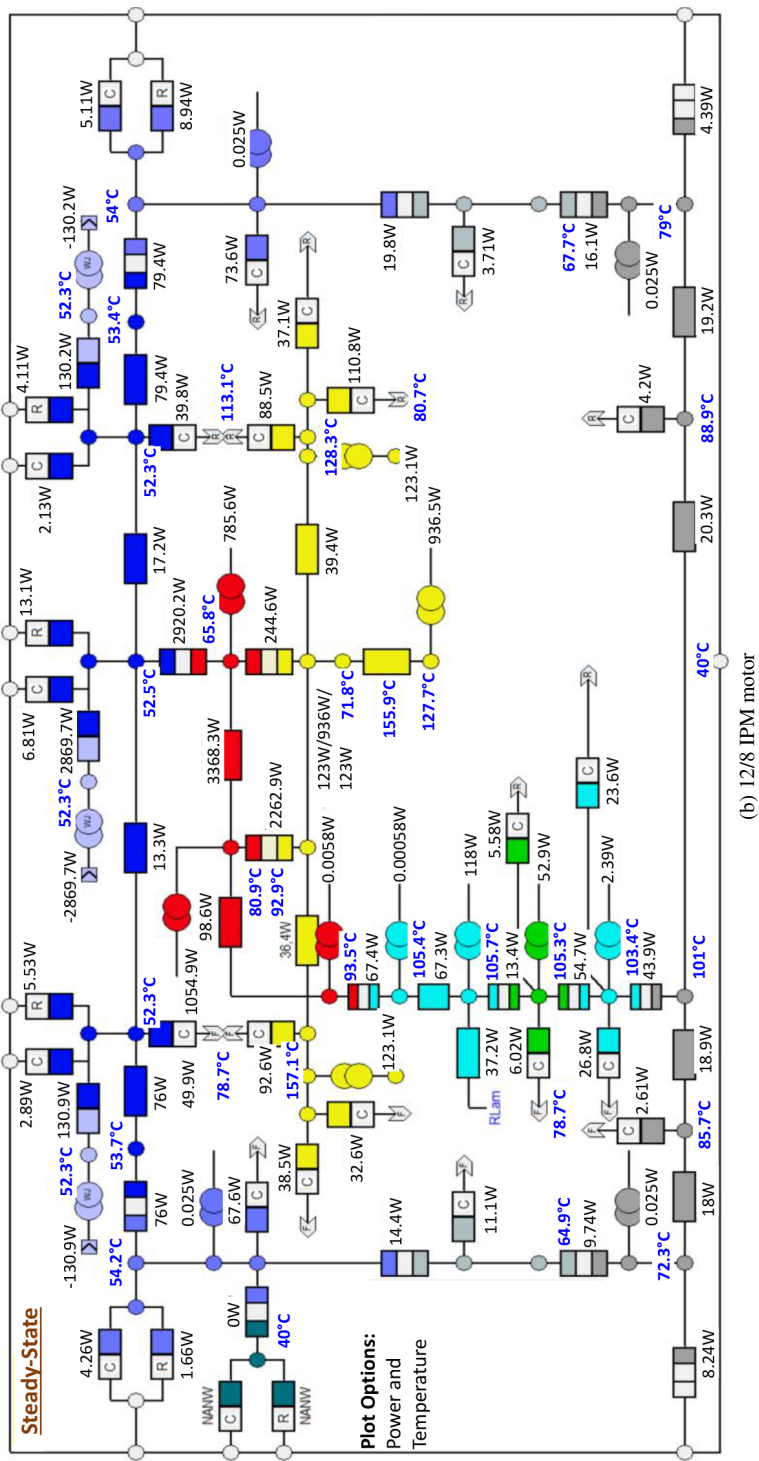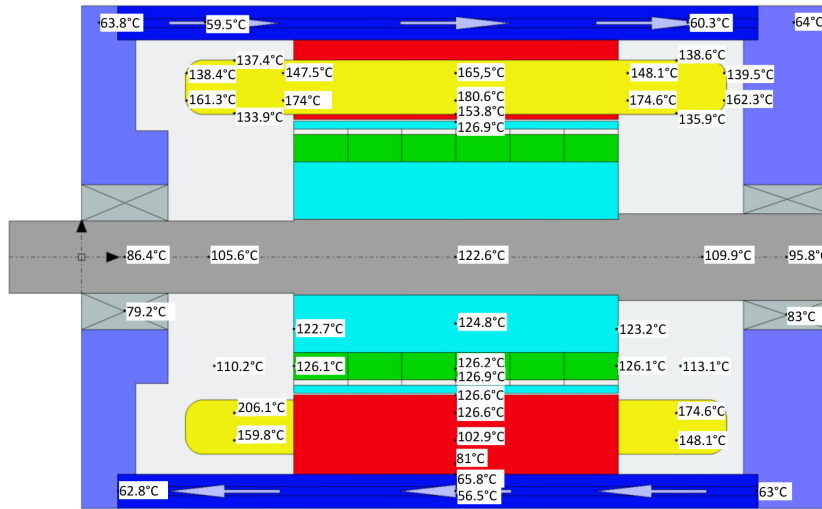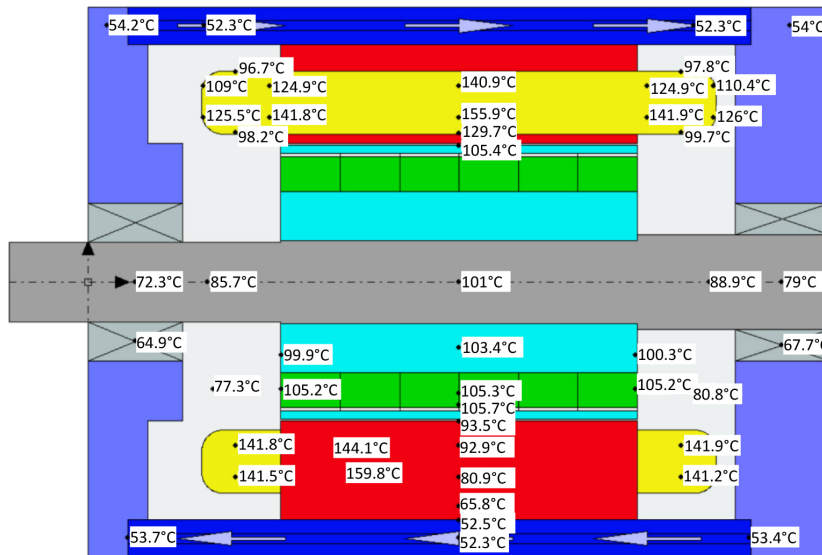
(a) 30/8 IPM motor

Fig. 11. Thermal network analysis with the thermal resistances, power flow through resistances, and nodal temperatures at nominal operating point: 30/8 IPM motor (a); 12/8 IPM motor (b)

(b) 12/8 IPM motor

The most appropriate algorithms used to calculate convection heat transfer and pressure drops are set up in the numerical calculation. Thermal resistances for the conduction heat transfer paths are calculated from the dimensions and thermal conductivity of each component of the motor. Radiation, in turn, is computed from emissivity and view factor coefficients and component

(a) 30/8 IPM motor

(b) 12/8 IPM motor

Fig. 12. Axial temperature distribution at the nominal operating point:
30/8 IPM motor (a); 12/8 IPM motor (b)

surface area [35, 38, 39]. Based on the data on temperature loss, and on the velocity distribution of the cooling fluid in the cooling channels depending on the machine, the thermal flux values were determined and the distribution of these values in components of the electric machine were computed. The steady-state thermal network based on motor geometry and type of cooling with regard to the power dissipated on individual elements is shown in Fig. 11. The thermal network consists of thermal resistance, power sources, thermal capacitances, nodal temperatures and power flow through resistances. The steady-state schematic diagram presented below is an accessible illustration of temperature distribution in regions such as the rotor (turquoise) and stator core (red), windings (yellow), magnets (green), housing (blue), and motor shaft (grey). For example, it can be observed that the main component of resistance between housing and stator back iron is due to the effective interface gap. In addition, the temperature of the housing and stator back iron of the DW motor is marked at the node and is 65.8°C and 81°C, respectively. In the case of the CW motor, these temperature values are 52.5°C and 65.8°C, respectively.

The performed thermal analysis shows the possibilities of the prototypes' operation. The presented three-dimensional illustration of the main heat transfer paths within an IPM motor shows that the 30/8 variant of the motor requires better cooling to maintain the required parameters of the motor's performance (without having to modify the magnetic circuit or the size of the machine). From the axial temperature distribution shown in Fig. 12, it is clear that in the 30/8 design, there is a significant problem with the acceptable temperature of the stator windings (especially inside the stator slot) at the required load torque at 4 500 rpm. The maximum value of the stator winding temperature that can be reached is 180°C. This unfortunately prevents the loading of the motor with a torque of 170 N·m in a long-term operation. What is more, an increase in losses in magnets beyond the nominal speed may lead to a partial demagnetization of the magnets.

It is clear from the above temperature investigation that the winding is the primary source of heat in the investigated electrical machines. As shown in Fig. 13, the coils of the concentrated winding located in the lower slot (near the air gap) are the most exposed to heat damage.
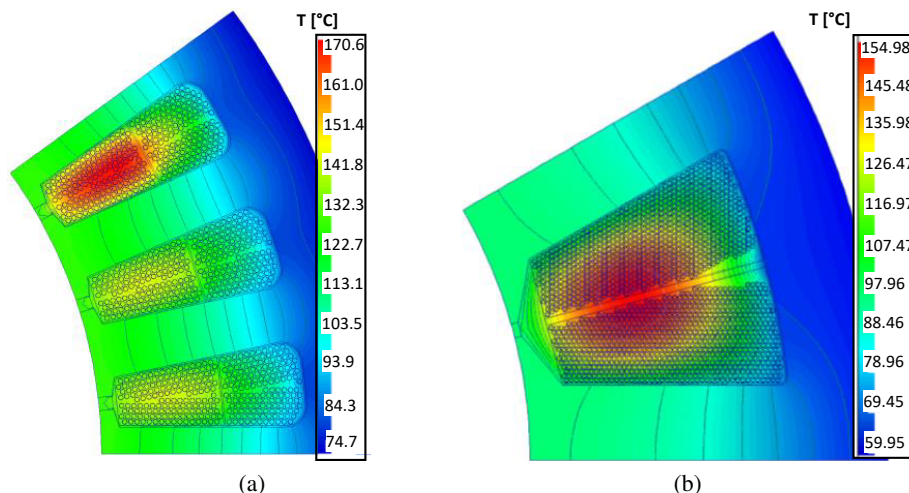

Fig. 13. Stator temperature distribution at the nominal operating point in a selected magnetic circuit geometry: 30/8 IPM motor (a); 12/8 IPM motor (b)

An additional thermal analysis concerns the assumption of limiting the maximum temperature of the stator winding to 180°C and of permanent magnets to 140°C. Assuming the adopted thermal limitations, the motor's parameters were determined under the analyzed cooling conditions, mentioned at the beginning of this chapter. Figures 14(a) and 14(b) show the variability of the shaft torque and output power, respectively, as a function of the rotational speed for both motor designs.

Table 2 summarizes the parameters obtained at the rated speed (4 500 rpm) and the maximum speed (11 000 rpm).

Table 2. Comparison of the obtained parameters of the prototype IPM with DW and CW

| Parameter	IPM with DW	IPM with CW	Unit
Rated speed 4 500 rpm			
Output power	79.99	80.07	kW
Torque ripple	3.1	6.6	%
System efficiency	95.5	96.3	%
Torque constant	0.5744	0.5642	N·m/A
Copper loss (DC+AC)	1 888	1 152	W
AC copper loss	654	248	W
Iron loss	1 792	1 442	W
Magnet loss	12.1	55.9	W
Magnet temperature	126.2	105.3	°C
Winding temperature (avg)	153.7	127.6	°C
Winding temperature (max)	180.6	155.9	°C
Maximum speed 11 000 rpm			
Output power	44.5	48	kW
Torque ripple	20	13	%
System efficiency	89.9	93.7	%
Torque constant	0.23	0.26	N·m/A
Copper loss (DC+AC)	1 787	626	W
AC copper loss	1 359	387	W
Iron loss	3 254	2 369	W
Magnet loss	33.2	580	W
Magnet temperature	136.5	140	°C
Winding temperature (avg)	144.7	107	°C
Winding temperature (max)	180	130	°C
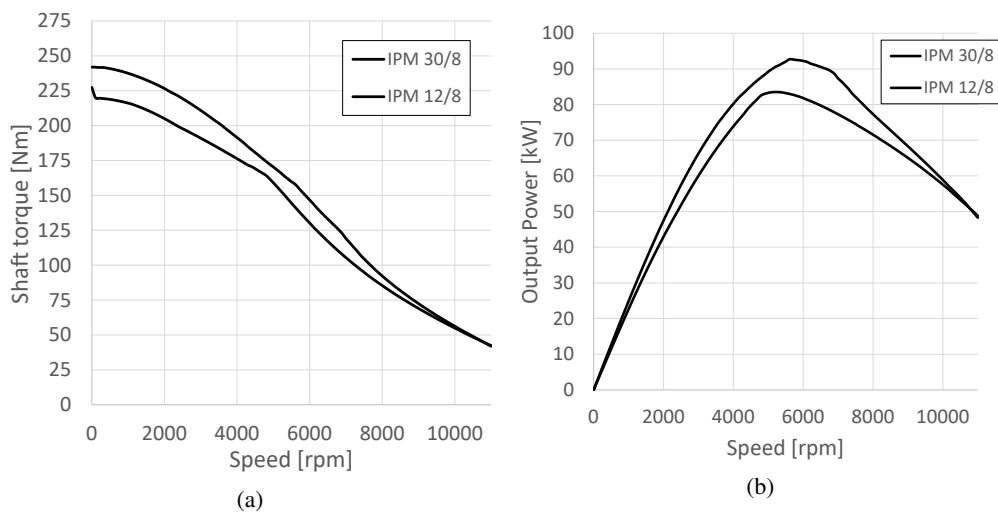
Fig. 14. Comparison of the motors with DW and CW with thermal requirements for stator winding and permanent magnet: shaft torque vs. speed (a); output power vs. speed with thermal requirements for stator winding and permanent magnet (b)

6. Conclusions

The study aimed to compare two brushless IPM motors used in high-power electric vehicles. These motors differ in the number of slots per pole, and a significant difference concerns the stator where concentrated winding (12/8) was used in the first design and distributed winding (30/8) in the second. The use of multi-wire winding reduces the effective slot filling factor. AC losses, which increase in constant power operation, have a significant influence on motor parameters. Both projects aimed at achieving the required electromagnetic torque (170 N·m). These assumptions were successfully met, which was confirmed by the results of calculations and tests presented in Chapters 2 and 4. In the range of constant torque operation, the 30-slot/8-pole structure is found to have a lower ripple of the electromagnetic torque (Fig. 6(b)). When the electric machine enters the field weakening zone, torque ripple begins to rise. At a speed of 11 000 rpm, the 12-slot/8-pole motor design has a lower torque ripple (Table 2).

Both rotors are structurally adapted to work at a maximum rotational speed of 11 000 rpm with a large margin of the safety factor (above 3), see Chapter 4. In terms of thermal limitations, it can be seen that the 12/8 IPM motor structure meets the stated requirements much better (compared with the 30/8 structure), and it can work continuously with the required power of 80 kW at the required operating point (and the speed range can be extended from the base speed of 4 500 rpm to around 7 800 rpm without losing the required power). The calculation results show that under the assumed cooling conditions of the 12/8 concentrated winding design, it is not possible to obtain a power of 80 kW at a speed of 11 000 rpm. Therefore, this power was reduced to 48 kW. In turn, the 30/8 design has much worse operating parameters. The AC losses were significantly higher in the 30/8 machine, which was the reason, why the maximum winding temperature significantly

limited the machine's output power. In the case of the 12/8 motor in constant power operation, the temperature of the magnets was the main reason for the reduction of the maximum achievable power output. The use of parallel branches in the winding is more advantageous (more turns with fewer wires in the bundle rather than one branch with fewer turns and more wires in the bundle). The above conclusions indicate that the use of concentrated windings is more advantageous due to thermal aspects and allows to obtain greater power on the machine shaft for the same operating conditions of the motor.

Acknowledgements

References

[1] Koc M., Emiroglu S., Tamyurek B., *Analysis and simulation of efficiency optimized IPM drives in constant torque region with reduced computational burden*, Turkish Journal of Electrical Engineering and Computer Sciences, vol. 29, pp. 1643–1658 (2021), DOI: 10.3906/elk-2005-152.

[2] Qiu H., Zhang Y., Yang C., Yi R., *Performance analysis and comparison of PMSM with concentrated winding and distributed winding*, Archives of Electrical Engineering, vol. 2, no. 69, pp. 303–317 (2020), DOI: 10.24425/aee.2020.133027.

[3] Ogbuka C.U., Nwosu C., Agu M., *Dynamic and steady state performance comparison of line-start permanent magnet synchronous motors with interior and surface magnets*, Archives of Electrical Engineering, vol. 65, no. 1, pp. 105–116 (2016), DOI: 10.1515/aee-2016-0008.

[4] Liu X., Li Y., Liu Z., Ling T., Luo Z., *Optimized design of a high-power-density PM-assisted synchronous reluctance machine with ferrite magnets for electric vehicles*, Archives of Electrical Engineering, vol. 66, no. 2, pp. 279–292 (2017), DOI: 10.1515/aee-2017-0021.

[5] Kwon S.O., Kim S.I., Zhang P., Hong J.P., *Performance comparison of IPMSM with distributed and concentrated windings*, Industry Applications Conference, Tampa, USA, pp. 1–5 (2006), DOI: 10.1109/IAS.2006.256807.

[6] Liu G., Gong W., Chen Q., Jian L., Shen Y., Zhao W., *Design and analysis of new fault-tolerant permanent magnet motors for four-wheel-driving electric vehicles*, IEEE Transactions on Magnetics, vol. 48, no. 11, pp. 4176–4179 (2012), DOI: 10.1063/1.3672853.

[7] Yamazaki K., Fukushima Y., Sato M., *Loss analysis of permanent-magnet motors with concentrated winding–validation of magnet eddy-current loss due to stator and rotor shapes*, IEEE Transactions on Industry Applications, vol. 45, no. 4, pp. 1334–1342 (2009), DOI: 10.1109/TIA.2009.2023393.

[8] Dutta R., Chong L., Rahman F., *Analysis and experimental verification of losses in a concentrated wound interior permanent magnet machine*, Progress in Electromagnetics Research B, vol. 48, pp. 221–248 (2013), DOI: 10.2528/PIERB12110715.

[9] Choe Y.Y., Oh S.Y., Ham S.H., Jang I.S., *Comparison of concentrated and distributed winding in an IPMSM for vehicle traction*, Energy Procedia, vol. 14, pp. 1368–1373 (2012), DOI: 10.1016/j.egypro.2011.12.1103.

[10] Gundogdu T., Komurgoz G., *Influence of winding configuration on the performance of surface-mounted PM machines*, International Journal of Mechanical Engineering and Robotics Research, vol. 6, pp. 46–49 (2017), DOI: doi.org/10.18178/ijmerr.6.1.46-49.

[11] Chevailler S., Feng L., Binder A., *Short-circuit faults in distributed and concentrated windings of PM synchronous motors*, European Conference on Power Electronics and Applications, Aalborg, Denmark, pp. 1–10 (2007), DOI: 10.1109/EPE.2007.4417416.

[12] Szelag W., Jedryczka C., *Analysis of multiphase synchronous machines with fractional slot concentrated windings*, Computer Applications in Electrical Engineering, vol. 14, pp. 231–244 (2016), DOI: 10.21008/j.1508-4248.2016.0021.

[13] El-Rafaie A.M., *Fractional-slot concentrated-winding synchronous permanent magnet machines: opportunities and challenges*, IEEE Transactions on Industrial Electronics, vol. 1, no. 57, pp. 107–121 (2010), DOI: 10.1109/TIE.2009.2030211.

[14] El-Rafaie A.M., Zhu Z.Q., Jahns T.M., Howe D., *Winding inductances of fractional slot surface-mounted permanent magnet brushless machines*, Edmonton, Canada, pp. 1–8 (2008), DOI: 10.1109/08IAS.2008.61.

[15] Papini F., Osama M., *Electromagnetic design of an interior permanent magnet motor for vehicle traction*, XIII International Conference on Electrical Machines, Alexandropoulis, Greece, pp. 1–7 (2018), DOI: 10.1109/ICELMACH.2018.8507222.

[16] Coenen I., Giet M., Hameyer K., *Quantitative comparison of electromagnetic performance of electrical machines for HEVs/EVs*, CES Transactions on Electrical Machines and Systems, vol. 1, pp. 37–47 (2017), DOI: 10.23919/TEMS.2017.7911107.

[17] Santiago J.D., Bernhoff H., Ekergard B., Eriksson S., *Electrical motor drivelines in commercial all-electric vehicles: a review*, IEEE Transactions on Vehicular Technology, vol. 61, pp. 475–484 (2012), DOI: 10.1109/TVT.2011.2177873.

[18] Ehsani M., Yimin G., Miller J.M., *Hybrid electric vehicles: architecture and motor drives*, Proceeding of IEEE, vol. 4, pp. 719–728 (2007), DOI: 10.1109/JPROC.2007.892492.

[19] Agamloh E., Jouanne A., Yokochi A., *An overview of electric machine trends in modern electric vehicles*, Machines, vol. 8, no. 2, pp. 1–16 (2020), DOI: 10.3390/machines8020020.

[20] Chu W.Q., Zhu Z.Q., Zhang J., Liu X., Stone D.A., Foster M.P., *Investigation on operational and efficiency map of electrically excited machines for electrical vehicle applications*, IEEE Transactions on Magnetics, vol. 51, no. 4, pp. 1–10 (2015), DOI: 10.1109/TMAG.2014.2359008.

[21] Zhang Z., Liu H., Song T., Zhang Q., Hu W., Liu W., *Performance evaluation of a 60kW IPM motor for medium commercial EV traction application*, CES Transactions on Electrical Machines and Systems, vol. 2, pp. 195–203 (2019), DOI: 10.30941/CESTEMS.2019.00026.

[22] Huynh T.A., Hsieh M.F., *Performance evaluation of permanent magnet motors using thin electrical steels*, IEEJ Journal of Industry Applications, vol. 6, pp. 422–428 (2017), DOI: 10.1541/ieejia.6.422.

[23] Kefalas T.D, Kladas A.G., *Thermal investigation of permanent-magnet synchronous motor for aerospace applications*, IEEE Transactions Industrial Electronics, vol. 61, no. 8, pp. 4404–4411 (2014), DOI: 10.1109/TIE.2013.2278521.

[24] Mlot A., Gonzalez J., *Performance assessment of axial-flux permanent magnet motors from a manual manufacturing process*, Energies, vol. 13, no. 8, pp. 1–15 (2020), DOI: 10.3390/en13082122.

[25] Mlot A., Kowol M., Kolodziej J., Lechowicz A., Skrobotowicz P., *Analysis of IPM motor parameters in an 80-kW traction motor*, Archives of Electrical Engineering, vol. 69, no. 2, pp. 467–481 (2020), DOI: 10.24425/aee.2020.133038.

[26] Mellor P., Wrobel R., Mlot A., Horseman T., Staton D., *Influence of winding design on losses in brushless AC IPM propulsion Motors*, IEEE Energy Conversion Congress and Exposition, Phoenix, USA, pp. 1–8 (2011), DOI: 10.1109/ECCE.2011.6064143.

[27] Godbehere J., Wrobel R., Drury D., Mellor P.H., *Salient PM rotor topology selection for a zero-speed injection based sensorless controlled machine*, IET International Conference on Power Electronics, Machines and Drives, Glasgow, UK, pp. 19–21 (2016), DOI: 10.1049/cp.2016.0316.

[28] Ma F., Yin H., Wei L., Tian G., Gao H., *Design and optimization of IPM motor considering flux weakening capability and vibration for electric vehicle applications*, Energies, vol. 10, no. 1533, pp. 1–15 (2018), DOI: 10.3390/su10051533.

[29] Mynarek P., Kolodziej J., Mlot A., Kowol M., *Influence of a winding short-circuit fault on demagnetization risk and local magnetic forces in V-shaped interior PMSM with distributed and concentrated winding*, Energies, vol. 14, no. 5125, pp. 1–16 (2021), DOI: 10.3390/en14165125.

[30] Kwon S., Kim S.I., Zhang P., Hong J.P., *Performance comparison of IPMSM with distributed and concentrated windings*, IEEE Industry Applications Conference, Forty-first IAS Annual Meeting, Florida, USA, pp. 1–5 (2006), DOI: 10.1109/IAS.2006.256807.

[31] Motor-CAD, www.motor-design.com.

[32] Volpe G., Popescu M., Marignetti F., Goss J., *Modelling AC Winding Losses in a PMSM with High Frequency and Torque Density*, IEEE Energy Conversion Congress and Exposition (ECCE), Portland, OR, pp. 1–6 (2018), DOI: 10.1109/ECCE.2018.8558065.

[33] Volpe G., Popescu M., Marignetti F., Goss J., *AC Winding Losses in Automotive Traction E-Machines: a New Hybrid Calculation Method*, IEEE International Electric Machines and Drives Conference (IEMDC), San Diego, CA, pp. 1–5 (2019), DOI: 10.1109/IEMDC.2019.8785409.

[34] Mellor P., Wrobel R., Simpson N., *AC losses in high frequency electrical machine windings formed from large section conductors*, IEEE Energy Conversion Congress and Exposition (ECCE), pp. 1–8 (2014), DOI: 10.1109/ECCE.2014.6954163.

[35] Mlot A., Korkosz M., Grodzki P., Lukaniszyn M., *Analysis of the proximity and skin effects on copper loss in a stator core*, Archives of Electrical Engineering, vol. 63, no. 2, pp. 211–225 (2014), DOI: 10.2478/aee-2014-0017.

[36] Xia Z.P., Zhu Z.Q., Wu L.J., Jewell G.W., *Comparison of radial vibration forces in 10-pole/12-slot fractional surface-mounted and interior PM brushless AC machines*, XIX International Conference on Electrical Machines, Rome, Italy, pp. 1–6 (2010), DOI: 10.1109/ICELMACH.2010.5608062.

[37] Han P.W., Choi J.H., Kim D.J., *Thermal analysis of high speed induction motor by using lumped-circuit parameters*, Journal of Electrical Engineering and Technology, vol. 10, pp. 2040–2045 (2015), DOI: 10.5370/JEET.2015.10.5.2040.

[38] Fan J., Zhang Ch., Wang Z., *Thermal analysis of permanent magnet motor for the electric vehicle application considering driving duty cycle*, IEEE Transactions on Magnetics, vol. 46, no. 10, pp. 2493–2496 (2010), DOI: 10.1109/TMAG.2010.2042043.

[39] Deaconu D.I., Ghita C., Chirila A.I., Navrapescu V., Popescu M., *Thermal study of induction machine using Motor-Cad*, 3rd International Symposium on Electrical and Electronics Engineering, Galati, Romania, pp. 1–5 (2010), DOI: 10.1109/ISEEE.2010.5628481.